Three-dimensional Elastic and Anelastic Structure of the Lowermost Mantle Beneath the Western Pacific From Finite-Frequency Tomography

Kensuke Konishi[1] [ID], **Nobuaki Fuji[2]** [ID], **and Frédéric Deschamps[1]** [ID]

[1]Institute of Earth Sciences, Academia Sinica, Taipei, Taiwan, [2]Université de Paris, Institut de Physique du Globe de Paris, CNRS, Paris, France

Abstract We build a finite-frequency tomography method that uses traveltime and amplitude data for obtaining 3-D maps of shear velocity (V_S) and seismic attenuation (measured with the quality factor Q). We then apply this method to recover the 3-D V_S and Q structures in the lowermost mantle beneath the western edge of the Pacific large low shear velocity province, using the S and ScS phases for 31 earthquakes that occurred underneath the vicinity of Tonga and Fiji regions. Our data set consists of the transverse components of 1,341 traces from the Japanese F-net seismic station network. The waveform data are applied with a band-pass filter in the period range of 12.5–200 s, corresponding to the frequency range of 0.005–0.08 Hz. Both V_S and Q are lower than those in the Preliminary reference Earth model (PREM) in the bottom depth range, with the lowest part being situated at the center of the region we sample. This feature is robust across a variety of inversion configurations. We then estimate possible temperature anomalies in this region from the obtained V_S and Q structures. Discrepancy between the temperature anomalies predicted by these two quantities suggests that explaining simultaneously V_S and Q anomalies in this region requires both temperature and chemical anomalies. Assuming that Q anomalies are a reliable proxy for temperature and that compositional anomalies primarily consist of an excess in iron oxide, we propose a possible thermal and compositional structure for this region.

1. Introduction

Global seismology, which investigates the internal structure of the Earth using seismic data, suggests the presence of two large low shear velocity provinces (LLSVPs) in the lowermost mantle beneath the Pacific and Africa (e.g., Houser et al., 2008; Kustowski et al., 2008; Panning & Romanowicz, 2006; Ritsema et al., 2011; Simmons et al., 2009; Takeuchi, 2012). The nature and origin of these structures are still controversial, and two end-member hypotheses, clusters of purely thermal plumes or thermochemical piles of hot, chemically distinct material, are usually advocated (e.g., Davies et al., 2012; Deschamps et al., 2015; Garnero et al., 2016).

To assess the validity of these hypotheses, a detailed exploration of the LLSVPs is needed. Shear velocity (V_S) is one of the seismic properties most frequently measured in global seismology. However, its expression is dependent on both temperature and chemical distributions and is insufficient to distinguish the individual contributions of these parameters. Additional physical properties are thus required to resolve the thermal and chemical structures from seismic signals. Because it strongly depends on temperature (e.g., Minster & Anderson, 1981), attenuation parameter, or equivalently the quality factor Q may provide key information to constrain the thermal field. Due to its high sensitivity to the amplitude of seismic waveforms, Q should be inverted for using not only traveltimes but amplitudes simultaneously.

As a first attempt, Konishi et al. (2017) conducted waveform inversion for 1-D radial models of V_S and Q at three different locations to establish constraints on the thermal and chemical properties at the western tip of the Pacific LLSVP. These three sets of radial models of V_S and Q showed substantial difference in both V_S and Q with respect to PREM. The central profiles, where the strongest deviations are observed, were interpreted as an image of the root of the chemically distinct Caroline plume. Konishi et al. (2017) data set suggested that more lateral variability may exist in this region and could be resolved and imaged with appropriate 3-D techniques.

Table 1
Earthquakes Used in This Study

Event #	Date (YYYY/MM/DD)	Latitude	Longitude	Depth	M_W	Global CMT id
1	2002 January 2	−17.63	178.84	680.8	6.1	010202E
2	2004 January 11	−16.27	−176.05	381.4	5.9	011104B
3	2000 May 4	−17.72	−178.31	539.8	6.4	050400 K
4	2003 May 19	−18.02	−178.42	578.5	5.9	051903B
5	2002 June 16	−17.65	−178.5	588.1	5.9	061602C
6	2002 August 9	−16.25	−175.85	381.3	6.1	080902B
7	2003 October 15	−17.84	−178.59	594.9	5.9	101503A
8	2002 October 17	−19.8	−178.23	621.9	6.1	101702C
9	2001 November 5	−17.12	−178.96	579.7	6.2	110501D
10	2002 December 28	−18.0	−178.4	635.5	5.8	122802A
11	2006 February 24	−17.94	−179.42	640.9	6.1	200602241415A
12	2006 June 9	−17.36	−178.62	585.9	6.1	200606090558A
13	2006 July 23	−17.97	−178.42	597.9	5.8	200607232050A
14	2007 March 23	−18.87	−178.24	644.6	5.8	200703232230A
15	2007 April 9	−20.0	−177.97	613.7	5.9	200704090224A
16	2007 May 6	−19.44	−179.04	690.8	6.5	200705062111A
17	2007 May 6	−19.31	−179.05	691.6	6.0	200705062201A
18	2007 May 13	−19.58	−179.03	694.9	5.8	200705131126A
19	2008 April 18	−17.26	−178.98	577.8	6.3	200804182039A
20	2008 June 15	−17.77	−179.66	623.6	5.9	200806150113A
21	2008 December 17	−17.77	−178.3	547.8	5.8	200812171055A
22	2009 January 26	−17.83	−178.55	616.5	5.8	200901261154A
23	2009 January 27	−17.81	−178.51	612.7	5.9	200901270629A
24	2009 March 5	−17.46	−178.9	553.3	5.9	200903051933A
25	2009 November 22	−17.72	−178.36	546.4	6.3	200911220748A
26	2010 June 22	−19.16	−177.49	587.4	5.8	201006222216A
27	2011 April 3	−17.65	−178.45	562.3	6.4	201104031407A
28	2011 August 19	−16.52	−176.73	415.0	6.2	201108190354A
29	2011 October 27	−17.98	−179.4	608.7	6.0	201110270015A
30	2012 February 10	−17.98	−178.42	598.0	5.9	201202100147A
31	2013 November 23	−17.09	−176.38	386.6	6.5	201311230748A

The complexity of the localized structure of V_S in the western Pacific has already been investigated in a number of studies (e.g., He & Wen, 2009; Takeuchi et al., 2008; To et al., 2005). Existence of a localized 3-D heterogeneity in V_S has also been suggested (Konishi et al., 2014). So far, however, no detailed 3-D structure of Q has been inferred in this region. In this work, we extend the waveform analysis of Konishi et al. (2017) to finite-frequency tomography for a 3-D structure of both V_S and Q using traveltimes and amplitudes instead of full waveform, which eventually allowed us to observe the Q structure at a greater level of complexity than that obtained from 1-D radial models.

2. Data

The data set used for our 3-D inversion is essentially similar to that of Konishi et al. (2017). We use broadband seismic waveform data obtained from the Japanese F-net seismic station network (77 stations) for 31 deep earthquakes (Table 1) that occurred in the vicinity of Tonga and Fiji regions. The data set consists of 1,341 velocity seismograms. The geometry of the seismic sources and stations is plotted in Figure 1, including the projected raypaths of direct S waves.

AGU
100
ADVANCING EARTH
AND SPACE SCIENCE

Journal of Geophysical Research: Solid Earth
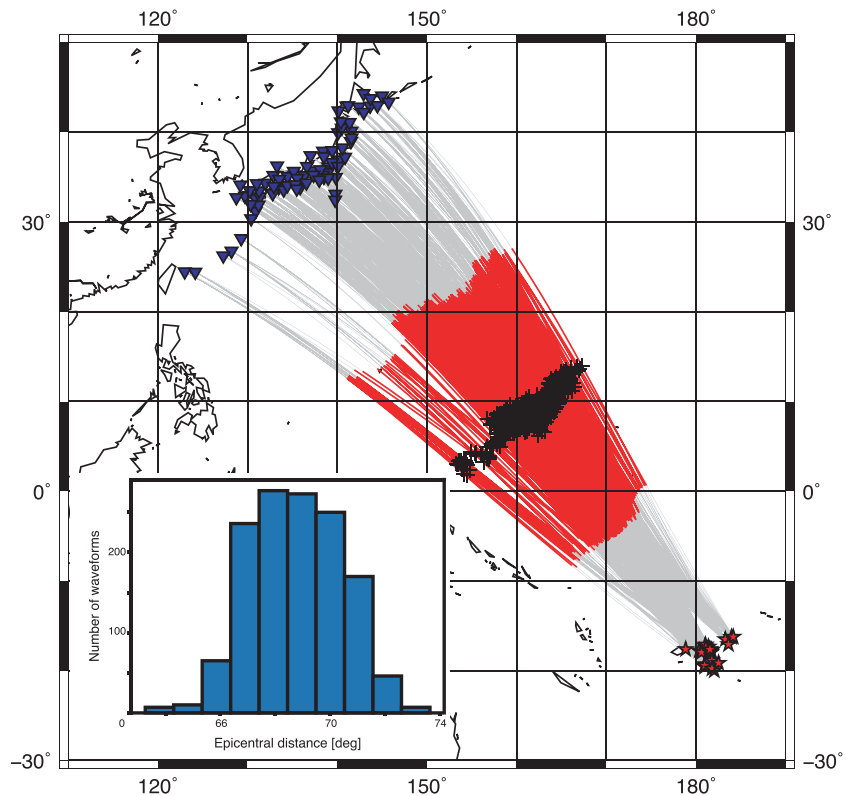
10.1029/2019JB018089

Figure 1. Geometry of the seismic events (red stars) and stations (blue triangles). Gray curves show the raypaths of direct *S* waves. The red parts on the raypaths denote the regions where the raypaths travel within the target depth range of this study. The black crosses indicate the bottoming points of the raypaths. The histogram shows the distribution of epicentral distances of the raypaths.

The histogram in Figure 1 shows the distribution of epicentral distances between the sources and receivers. Note that our data set does not include any waveforms with *S* wave traveling deeper than a depth of 2,000 km (900 km above the core-mantle boundary, CMB).

We deconvolve the instrument response and construct a data set consisting of the transverse component waveforms obtained by rotating the N-S and E-W components. Each waveform in our data set comprises primarily *ScS* wave (*S* wave reflected at the core-mantle boundary) and its precursors.

3. Methodology

We use a finite-frequency tomography method based on traveltime and amplitude of *ScS* phases, instead of full-waveform inversion, in order to obtain robust results to infer the 3-D elastic and anelastic structure beneath the western Pacific. In this section, we describe the data processing and inversion procedures.

3.1. Initial Model, Attributes Measurement

The initial model used in the inversion is defined as the average of the three 1-D models obtained in Konishi et al. (2017) and is represented in Figure 2. Synthetic waveforms are computed using the Direct Solution Method (Geller & Ohminato, 1994; Geller & Takeuchi, 1995) up to 0.3 Hz. The source parameters (moment tensors and centroid) are provided by the Global Centroid-Moment-Tensor Project, and we convolved the moment rate function.

We apply a band-pass filter to the waveforms with a frequency range of 0.005 to 0.08 Hz. In order to correct for the shallow region and source effects (static corrections), waveforms are aligned by *S* wave peaks and normalized by the amplitude of *S* phase. We then invert anomalies in traveltimes ($\delta\mathcal{T}$) and amplitudes ($\delta \ln A$) of the *ScS* phase between the observed and synthetic data for anomalies in shear velocity and attenuation. Note that because they do not propagate deeper than 2,000 km, all *S* waves in our data set do not travel through the target depth range. In addition, we assume that *S* and *ScS* waves for a same station-source pair
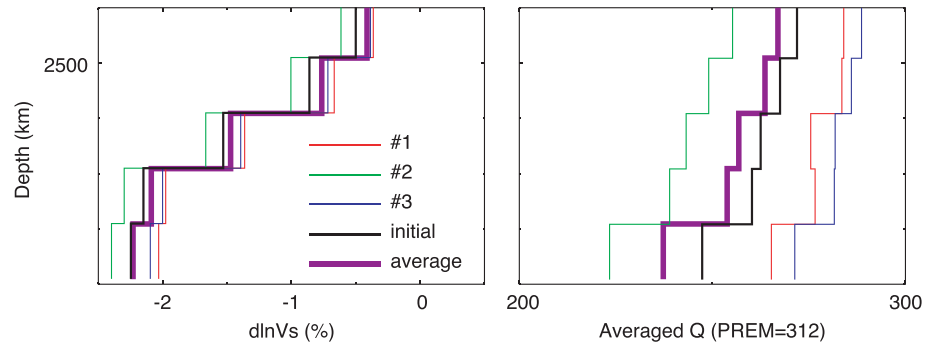
Figure 2. Radial profiles of V_S anomalies (d ln V_S) with respect to PREM (left) and Q (right) from the waveform inversions in Konishi et al. (2017). Labels #1 to #3 indicate the profile obtained with the western, central, and eastern paths subsets, respectively. The averaged structure of these profiles is plotted by the black lines and is used as an initial model for this study. Averaged radial structure of our preferred model (Figure 4) is denoted by the thick purple lines.

travel through a similar path in the shallow depth range. An important point to note is that the S waves in our data set do not have significant variance between data and synthetics using PREM Konishi et al. (2017). In particular, these variations are much smaller than variations in ScS waves in the lowermost mantle (i.e., our target depth range).

The 3-D model is horizontally parametrized on $5° \times 5°$ grids (equivalent to approximately 300×300 km at the CMB) with a vertical step of 100 km from the CMB up to 500 km above the CMB. We choose this parameterization due to the higher sensitivity of ScS phases to the vertical structure than to the horizontal structure. The horizontal distribution of the grid points is shown in Figure 3.

3.2. Partial Derivatives for V_S and Q

The formulation of the partial derivatives for both elasticity (μ) and anelasticity (Q) (and their Jacobians) is written in section 2.1.2 of Fuji et al. (2010). Here we briefly summarize this formulation. First, the frequency dependence of μ is given by Azimi et al. (1968) following:

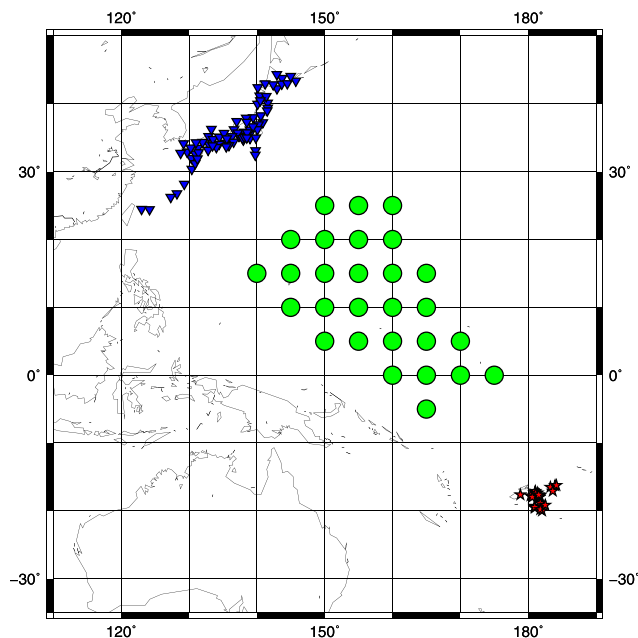$$\mu(\omega) \approx \mu_0 \left(1 + \frac{2q \ln(\omega/\omega_0)}{\pi} \right) (1 + iq), \tag{1}$$

Figure 3. Horizontal parametrization (28 green circles).

where $i = \sqrt{-1}$, $q = Q^{-1}$, ω is the angular frequency, ω_0 is the reference angular frequency (here taken at $\omega_0 = 2\pi$, i.e, a reference frequency of 1 Hz), and μ_0 is the real part of the elastic parameter $\mu(\omega_0)$. Differentials of $\mu(\omega)$ and waveform u are given by

$$\delta\mu(\omega) = \frac{\partial\mu(\omega)}{\partial\mu_0}\delta\mu_0 + \frac{\partial\mu(\omega)}{\partial q}\delta q, \tag{2}$$

$$\delta u_T = \frac{\partial u_T}{\partial\mu(\omega)}\frac{\partial\mu(\omega)}{\partial\mu_0}\delta\mu_0 + \frac{\partial u_T}{\partial\mu(\omega)}\frac{\partial\mu(\omega)}{\partial q}\delta q, \tag{3}$$

and

$$\delta u_T(\omega) = \frac{\partial u_T}{\partial\mu(\omega)}\left(1 + \frac{2q\ln(\omega/\omega_0)}{\pi}\right)(1 + iq)\delta\mu_0 + \frac{\partial u_T}{\partial\mu(\omega)}\mu_0\left[\frac{2\ln(\omega/\omega_0)}{\pi} + i\left(1 + \frac{4q\ln(\omega/\omega_0)}{\pi}\right)\right]\delta q. \tag{4}$$

This formulation thus defines perturbation from the partial derivatives with respect to our target parameters μ_0 and q. Note that we compute the partial derivative $\partial u/\partial\mu(\omega)$ using the algorithm of Geller and Hara (1993):

$$\left(\frac{\partial u_T(\omega)}{\partial\mu(\mathbf{r})}\right)^* \delta\mu(\mathbf{r}) = -\frac{1}{2}\left\{u_{r,s}(\mathbf{r}) + u_{s,r}(\mathbf{r})\right\}^*[\eta_{s,r}(\mathbf{r}) + \eta_{r,s}(\mathbf{r})]\delta\mu, \tag{5}$$

where $\mathbf{r}$ denotes the location of a perturbation and u_r and η_r denote the r component of the displacement and of the back-propagated displacement by a point force in the transverse direction at a station, respectively. The summation convention, summation over the repeated subscripts, is used. The subscript $_s$ denotes spatial differentiation with respect to the s coordinate. Using the relation between the perturbation to V_S and μ,

$$2\rho V_S\delta V_S = \delta\mu_0, \tag{6}$$

we obtain:

$$\delta u_T(\omega) = 2\rho V_S\frac{\partial u_T}{\partial\mu(\omega)}\left(1 + \frac{2q\ln(\omega/\omega_0)}{\pi}\right)(1 + iq)\delta V_S + \frac{\partial u_T}{\partial\mu(\omega)}\mu_0\left[\frac{2\ln(\omega/\omega_0)}{\pi} + i\left(1 + \frac{4q\ln(\omega/\omega_0)}{\pi}\right)\right]\delta q. \tag{7}$$

3.3. Inverse Problem

We conduct finite-frequency tomography for V_S and Q by inverting measured traveltime ($\delta\mathcal{T}$) and amplitude ($\delta\ln A$). We define the cost function to minimize as follows:

$$\|\mathbf{d} - \mathbf{G}\boldsymbol{\delta}\mathbf{m}\|^2, \tag{8}$$

where $\mathbf{d}$ consists of the set of $\delta\mathcal{T}$ and $\delta\ln A$ measured within all the waveforms in the data set and $\mathbf{G}$ is a kernel matrix with respect to model perturbations $\delta\mathbf{m}$ (V_S and q). In order to have finite-frequency kernels, we first compute partial derivatives of full-waveform (K^u) with respect to δV_S and δq. A kernel for full-waveform u_T (K^u) is converted in kernels for traveltime $\mathcal{T}$ ($K^{\mathcal{T}}$) and amplitude $\ln A$ ($K^{\ln A}$), respectively, as follows:

$$K_Y^X(\mathbf{r_Q}) = \int_{t_1}^{t_2} J^X(\mathbf{r_R}, t; \mathbf{r_S})K_Y^u(\mathbf{r_Q}, t)\mathrm{d}t, \tag{9}$$

$$J^{\mathcal{T}}(\mathbf{r_R}, t; \mathbf{r_S}) = -\frac{\partial_t u_T(\mathbf{r_R}, t; \mathbf{r_S})}{\int_{t_1}^{t_2}|\partial_t u_T(\mathbf{r_R}, t; \mathbf{r_S})|^2\mathrm{d}t}, \tag{10}$$

and

$$J^{\ln A}(\mathbf{r_R}, t; \mathbf{r_S}) = \frac{u_T(\mathbf{r_R}, t; \mathbf{r_S})}{\int_{t_1}^{t_2}|u_T(\mathbf{r_R}, t; \mathbf{r_S})|^2\mathrm{d}t}, \tag{11}$$

where X indicates data type (either $\mathcal{T}$ or $\ln A$) and Y indicates the model parameter (either V_S or q), respectively. Difference in the maximum amplitudes of the partial derivatives with respect to the two model parameters (V_S or q) is taken into account as follows:

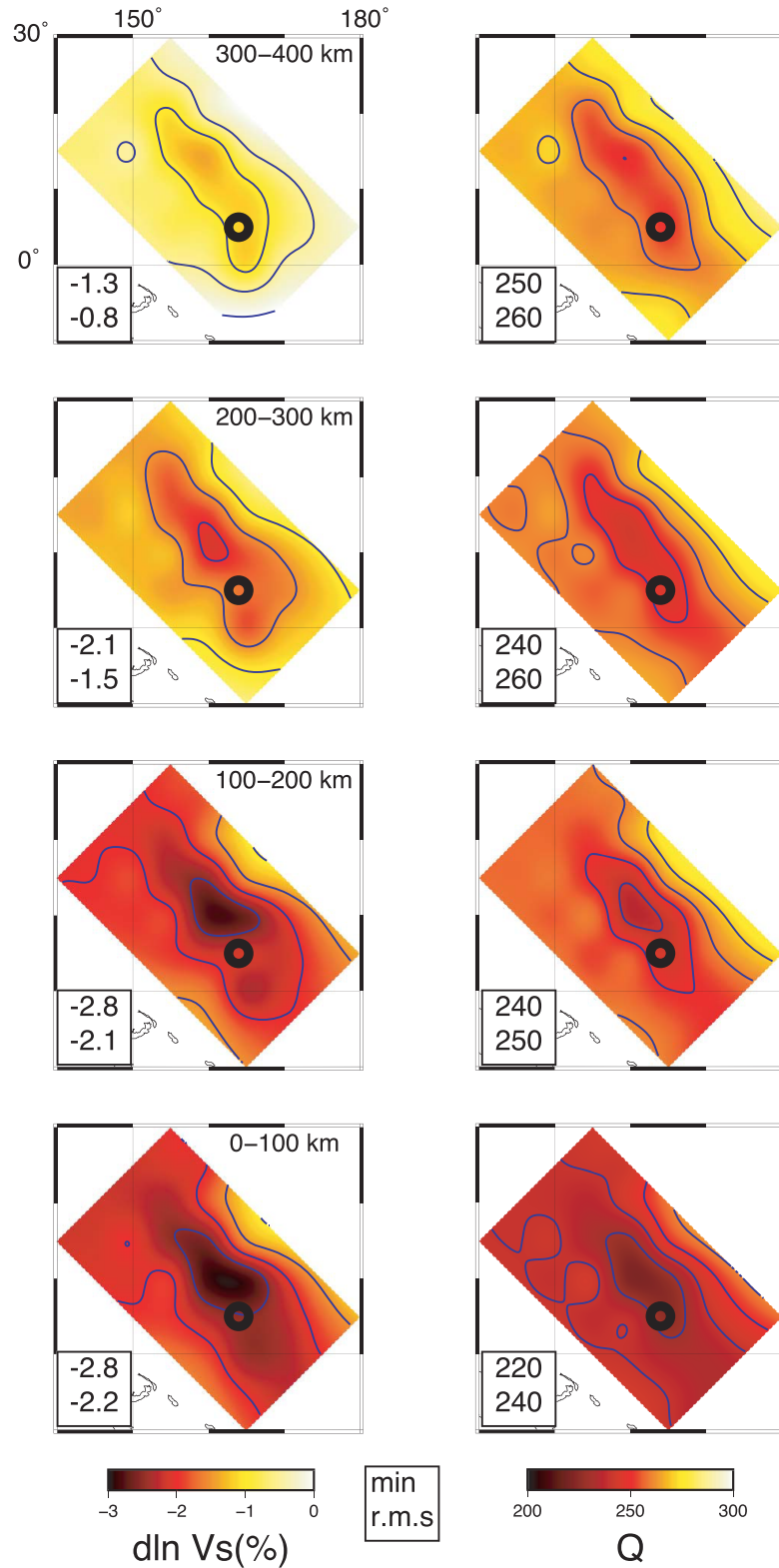$$\mathbf{G}' = \left(\mathbf{G}_{V_S}|a\mathbf{G}_q\right), \tag{12}$$

Figure 4. Our preferred model. For each depth range, $d \ln V_S$ and Q are displayed on the left and right columns, respectively, with a contour interval of 0.5% in $d \ln V_S$ and 10 in Q. The top right insets on $d \ln V_S$ maps indicate elevation above the CMB. The bottom left insets indicate the rms and lowest values in $d \ln V_S$ and Q. The thick black circle shows the surface location of the Caroline plume.

where a is the weighting for the elements of the kernel matrix $\mathbf{G}$ with respect to δq, since kernels $\mathbf{G}_{V_S}$ and $\mathbf{G}_q$ for V_S and q may not be totally independent/orthogonal. Behavior of results upon a variety of a values is discussed in Fuji et al. (2010), and we explore the influence of this value in section 4.2.

To control damping and smoothing in the inversion, we add two terms into equation (8). First, we consider the most general damping with $\mathbf{Wm}$, which adjusts the relative weights of the damping on V_S and q. In addition, we control smoothness in model with the term $\mathbf{Xm}$. The objective cost function is then

$$\|\mathbf{d} - \mathbf{Gm}\|^2 + \gamma\|\mathbf{Wm}\|^2 + \xi\|\mathbf{Xm}\|^2, \tag{13}$$

where γ and ξ are two constants controlling the amount of damping and smoothing, respectively, and, $\mathbf{W}$ and $\mathbf{X}$ are given by

$$\mathbf{W} = \{w_{ij}\} = \begin{matrix} w_V & i = j, m_i \to V_S \\ w_q & i = j, m_i \to q \\ 0 & i \neq j \end{matrix}, \tag{14}$$

$$\mathbf{X} = \begin{pmatrix} y_{12} & -y_{12} & 0 & \dots & 0 & 0 \\ y_{13} & 0 & -y_{13} & \dots & 0 & 0 \\ & \vdots & & \ddots & & \\ 0 & y_{23} & -y_{23} & \dots & 0 & 0 \\ & \vdots & & \ddots & & \\ 0 & 0 & 0 & \dots & y_{n-1n} & -y_{n-1n} \end{pmatrix}. \tag{15}$$

$\mathbf{Xm}$ represents formula of the relations between m_i and m_j for all $i, j (i \neq j)$, which controls the smoothness between m_i and m_j. The weighting factors y_{ij} are functions of the locations of m_i and m_j that control the amount of smoothing. In this study, the smoothing factor is defined by

$$y_{ij} = \frac{100}{100 + |z_i - z_j|} \frac{100^2}{|\mathbf{x}_i - \mathbf{x}_j|^2}, \tag{16}$$

where $\mathbf{x}_i$ is the geometrical coordinate of the location of ith (in superscript) point and z_i is the depth of the location of ith (in superscript) point. The first coefficient means that distance in the depth direction affects more strongly the smoothing factor. Note that a value of 100^2 is for the minimum value of $|\mathbf{x}_i - \mathbf{x}_j|^2$. Note also that the formula has the relation of m_i and m_j only if the perturbation types (i.e., elasticity or anelasticity) of the m_i and m_j are the same (i.e., $m_i, m_j \in \mathbf{m}_{V_S}$ or $m_i, m_j \in \mathbf{m}_q$).

Finally, a model $\mathbf{m}$ is calculated such that it minimizes the value of the cost function defined in equation (13) following:

$$\mathbf{m} = (\mathbf{G}^T\mathbf{G} + \gamma\mathbf{W}^T\mathbf{W} + \xi\mathbf{X}^T\mathbf{X})^{-1}\mathbf{G}^T\mathbf{d}. \tag{17}$$

4. Seismological Model

4.1. Preferred Model

Figure 4 shows our preferred model, obtained with the following parameters: $a = 3,333^{-1} (= a_0), \gamma = 0.086 (= \gamma_0)$, and $\xi = 358 (= \xi_0)$ (the definition and influence of each regularization parameter are discussed in section 4.2). Root-mean-square and minimum values in $d \ln V_S$ and Q at each depth range are indicated in inset. Throughout the region covered by our model, both V_S and Q are substantially lower than the PREM values. The difference between the obtained model and PREM becomes smaller as the depth range goes shallower. In the lowermost layer, $d \ln V_S$ peaks at -2.8% and Q reaches a minimum at 220, while at 400 km above the CMB $d \ln V_S$ is -1.3% and Q is 250. The pattern in V_S and Q anomalies is roughly similar, with the central region being slower and more attenuated (lower Q) than the surrounding regions, but they slightly differ in the details. Note that the contrast in $d \ln V_S$ between the center of the region and its surroundings is stronger in the shallower parts. Furthermore, the contrast in Q is visible at all the depth ranges, while $d \ln V_S$ is more homogeneous at the shallowest depths. Average values of both $d \ln V_S$ and Q in each depth range are shown in Figure 2.

4.2. Effects of Regularizations

We now investigate the stability of our model with respect to the amount of damping and smoothing. First, we vary the damping factor γ. Figure 5 shows a model obtained with a value of γ equal to twice that of our preferred model ($\gamma = 2 \times \gamma_0$), all other parameters values being the same; that is, $a = a_0, \xi = \xi_0, w_{V_S} = w_{V0}$, and $w_q = w_{q0}$. Maps in Figure 5 do not show significant differences compared to our preferred model.

Figure S1 in the supporting information further shows the result obtained with a value of γ equal to half that of our preferred model ($\gamma = \gamma_0/2$), all other parameters values being the same. Again, the observed pattern is similar to that of our preferred model.

We also implement the smoothing in our objective cost function. Here, we change the factor ξ, which controls the smoothing of both $d \ln V_S$ and Q. Figure 6 shows a model with a value of ξ equal to half the value used for our preferred model ($\xi = \xi/2$). Again, values of all other parameters are unchanged, that is, $a = a_0, \gamma = \gamma_0, w_{V_S} = w_{V0}$, and $w_q = w_{q0}$. Differences are larger than when modifying the damping but remain overall small. The biggest difference appears in the maps of $d \ln V_S$ in the shallowest part of our model, where the minimum $d \ln V_S$ observed in the center of the domain is more pronounced by about 0.1%. In addition, the distribution of Q is more contrasted. Incidentally, the outcomes obtained by increasing the weighting of Q alone are similar to that obtained by increasing the weighting of both V_S and Q.

As mentioned in section 3.1, we control difference in the maximum amplitudes of kernels with respect to V_S and q. We now examine the contribution of choices of the factor a in equation (12). Figure 7 shows a model obtained with a value of a 50% larger than in our preferred model ($a = 1.5 \times a_0$), while all other parameters are the same, that is, $\gamma = \gamma_0, \xi = \xi_0, w_{V_S} = w_{V0}$, and $w_q = w_{q0}$. Again, compared to our preferred model, we do not see significant differences in the structure and amplitudes of $d \ln V_S$. However, clear differences in the models of Q can be seen. In particular, the values of Q are slightly lower at all the depth range, by about 10–20. The Q pattern, by contrast, remains unchanged. Overall, the tests we conducted in this section indicate that the effects of regularization are limited; that is, the results of our inversion are robust with respect to regularization.

4.3. Robustness of Data

To assess the robustness of our data set, we conduct a bootstrap test. We prepare 100 sub–data sets out of our whole data set, each sub–data set containing 70% of the whole data set, in which 938 selected waveforms are randomly chosen. We then conducted inversions for the all sub–data sets and calculate the average and standard deviation of the results. Figure S2 shows the standard deviation of $d \ln V_S$ and Q. Overall, differences between the original and randomly selected sub–data sets are very small. Differences between the original and sub–data sets further increase with depth. In the bottom layer, the rms and maximum of differences are 0.025% and 0.041% for $d \ln V_S$ and 0.40 and 0.83 for Q. The largest differences are seen at the edges of the models. These bootstrap tests thus indicate that our data set is robust and is only affected by small uncertainties, a result that is likely related to the raypath coverage of our data set.

4.4. Validation in Data Domain

In this study, we searched for a model that minimizes deviation in the values of traveltime ($\mathcal{T}$) and amplitude ($\ln A$) as is written in equation (8). Furthermore, we imposed damping, smoothing, and control on the amplitude factor as is written in equation (17). To assess the quality of our results, we compared observed and modeled waveform data. Since we used finite-frequency tomography, it is worth looking at the improvement in data (full-waveform) domain. In order to quantify misfit between waveforms, we define variance of each waveform (var_i) and variance of all the waveforms (var), respectively, as below:

$$\mathrm{var}_i = \frac{\left\| \boldsymbol{u}_{\mathrm{obs},i} - \boldsymbol{u}_{\mathrm{syn},i} \right\|^2}{\left\| \boldsymbol{u}_{\mathrm{obs},i} \right\|^2}, \tag{18}$$

$$\mathrm{var} = \frac{\sum\limits_i \left\| \boldsymbol{u}_{\mathrm{obs},i} - \boldsymbol{u}_{\mathrm{syn},i} \right\|^2}{\sum\limits_i \left\| \boldsymbol{u}_{\mathrm{obs},i} \right\|^2}. \tag{19}$$

The values of the variance for all the waveforms versus observed waveforms (equation (19)) are 1.5 for PREM, 0.64 for the initial model, and 0.63 for our preferred model.
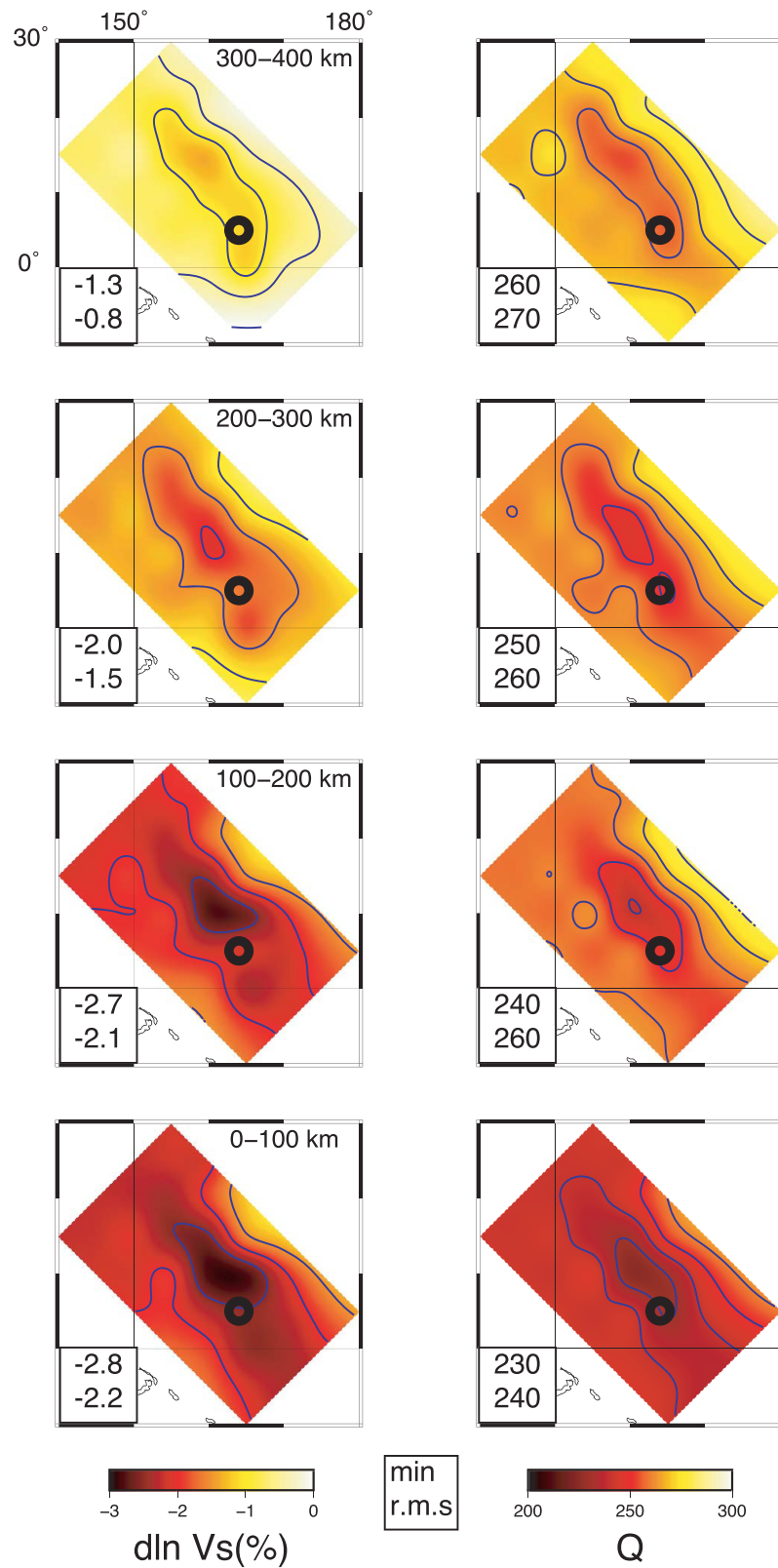
Figure 5. Models obtained with stronger weighting on both $d \ln V_S$ and Q. $a = a_0, \gamma = 2 \times \gamma_0, \xi = \xi_0, w_V = w_{V0}$, and $w_q = w_{q0}$. Legends and contour interval are the same as in Figure 4.
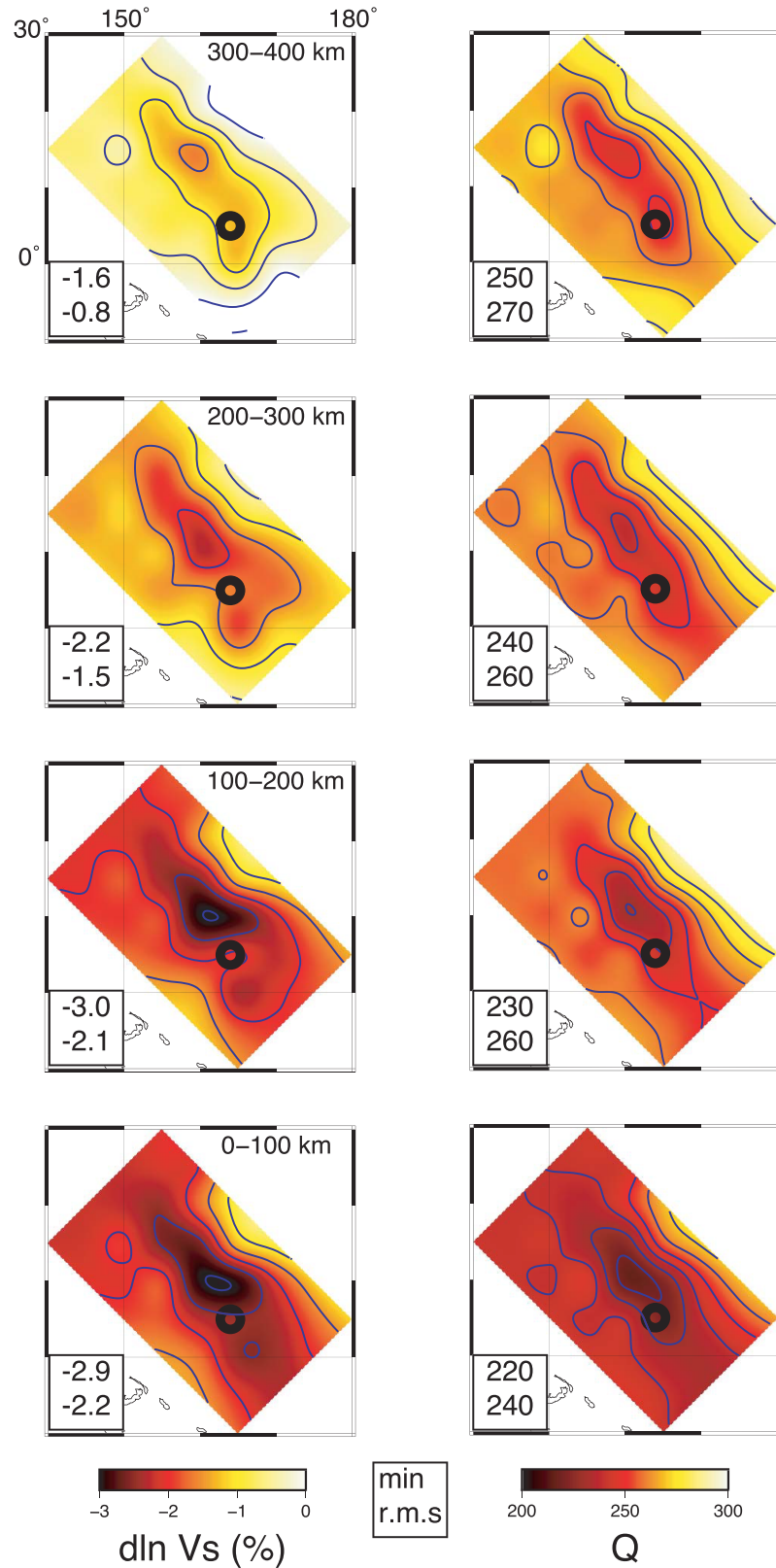
Figure 6. Models obtained with weak smoothing on both d ln V_S and Q. $a = a_0, \gamma = \gamma_0, \xi = 0.5 \times \xi_0, w_V = w_{V0}$, and $w_q = w_{q0}$. Legends and contour interval are the same as in Figure 4.
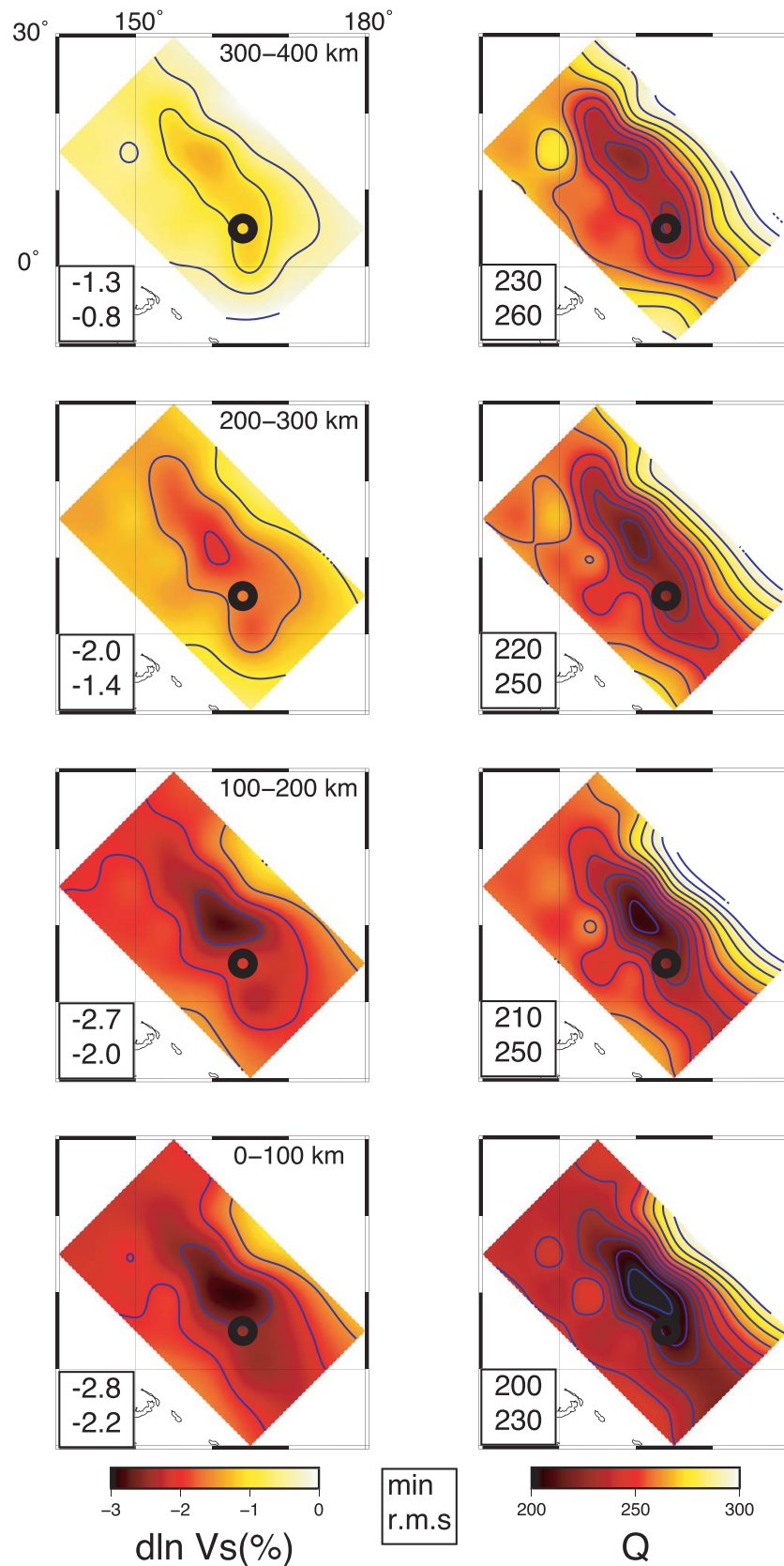
Figure 7. Models obtained with a larger value of a. $a = 1.5 \times a_0, \gamma = \gamma_0, \xi = \xi_0, w_V = w_{V0}$, and $w_q = w_{q0}$. Legends and contour interval are the same as in Figure 4.
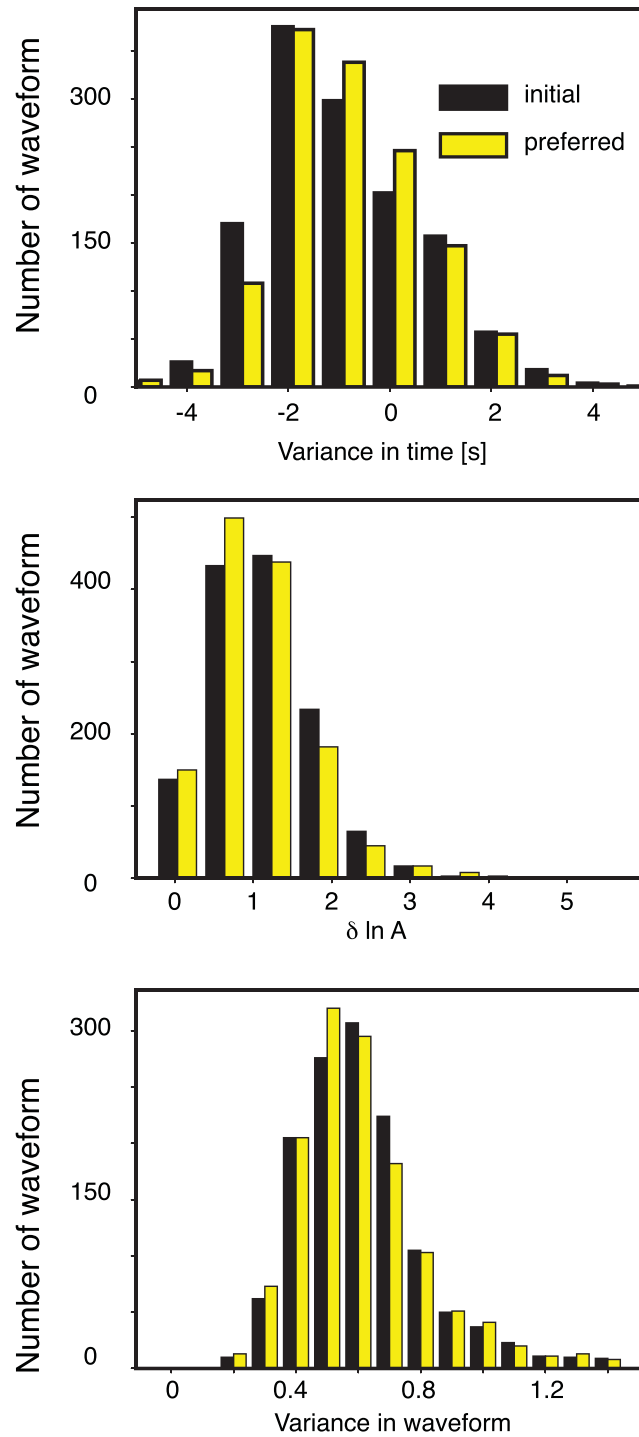
Figure 8. Distribution histograms of the variances in traveltime (top), amplitude (middle), and waveform (bottom) between the observed and synthetic waveforms computed with initial model (black) and the preferred model (yellow).

To assess improvements in individual waveforms, we plotted the distribution histograms of the variance values in $\delta\mathcal{T}$, $\delta\ln A$, and waveform (equation (18)) for each waveform in Figure 8. This plot shows that all the values are improved with using the preferred model.

We further performed comparisons of waveforms, as illustrated by Figure 9. The waveforms computed for the initial model and preferred model fit the observed *ScS* phase much better than the waveform computed for PREM.
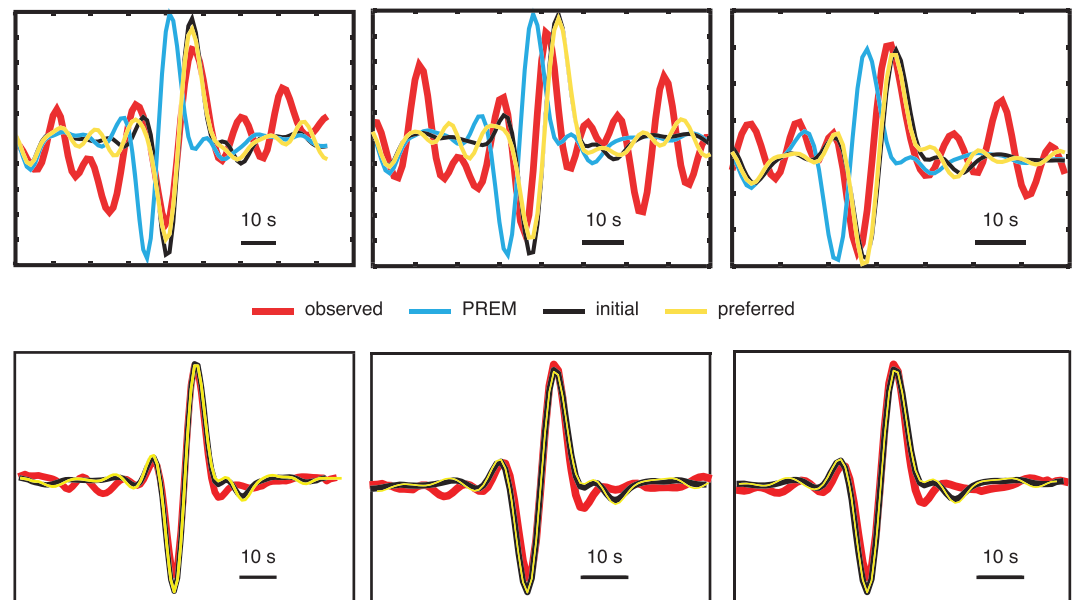
Figure 9. Upper panels: a comparison between observed waveforms, in red, and synthetic waveforms in blue, black, and yellow, computed via PREM, the initial model, and the preferred model, respectively. Lower panels: stacked waveforms of the seismic events from the upper panels.

While the improvement in individual waveforms from the initial model to the preferred model is not significant as that from PREM to our preferred model (Figure 9), the histogram shows a global improvement in both traveltime and amplitude (Figure 8).

It is however difficult to describe general modification in waveforms, partly because of the frequency band of the data set we used. In the leftmost and center panels, the fit in the first peak of *ScS* is improved with the preferred model, especially in terms of amplitude. By contrast, in the waveform plotted at the rightmost panel the phases at the latter part of *ScS* are well recovered.

Although we see some wiggles in the observed waveforms, these features disappear in the stacked waveforms (Figure 9). In this data set, most of the improvements are achieved for the main peaks of *ScS*.

4.5. Influence From Shallower Parts

We further examined possible influence from shallower regions of the mantle on our inversion. Konishi et al. (2014) have shown the pseudo-orthogonality of waveform partial derivatives with respect to V_S in the upper mantle and in the lowermost mantle. This implicitly supports our hypothesis that shear velocity perturbations in our waveform data set are localized in the lowermost mantle. Here, we further investigate the robustness of our inversion results by testing several possible cross-talk effects during inversions, including (i) static correction effects, (ii) simultaneous inversions for deep and shallow depths, and (iii) inversions only for shallow depths.

First, we conduct inversion for the data set without the static correction described in section 3.1. All the parameters in equation (13) are the same as those used to obtain our preferred model. The resulting model is shown in Figure S3. In comparison to the preferred model (Figure 4), the distribution of values Q is slightly flatter. However, the model still indicates the same value ranges both in d ln V_S and Q. Whether we apply the static correction or not, the subsequent models are not significantly different.

To evaluate the possible trade-off between shallower regions of the mantle and our target depth range, we performed an additional inversion where we added the shallower mantle as target. We calculate 1-D kernel for the shallower distance range and added it to the inversion. The 1-D kernel is built for every 100 km from a depth of 500 km above the CMB to the Earth surface. In this inversion, we kept 3-D parameterization in the lowermost part as it is in our preferred model. The lowermost 3-D model obtained in this inversion is shown in Figure S4. The 1-D model for the shallower part is shown in Figure S5, in which we also plot the 1-D averaged values of 3-D model in each depth range as well as the average value of the preferred model

in black. While we observe several unstable patterns around depths of 200 and 700 km, and the models obtained with kernels accounting for the shallow mantle are flatter than our preferred model (Figure 4), as in the inversion without the static correction, the pattern of both V_S and Q is similar and their average values in each layer are also same as those in the preferred model. This test therefore suggests that the trade-off between the shallower part and the target region is small. We then conducted an inversion with only 1-D kernel for the whole mantle depth range. The 1-D model (with 100 km step) in the whole mantle is shown in Figure S6. Compared to the model obtained using 1-D kernel for the shallower part and 3-D kernel for the target depth range, we observe no significant difference in both the shallower mantle and the target depth range, which further indicates that our model has no or very limited trade-off from the shallow mantle. Figure S7 plots 1-D models obtained for the shallow mantle only. This model has slightly different values in V_S compared to those obtained with the whole mantle kernels (i.e., including the target region), while Q is almost identical. However, at depths greater than 1,000 km, the difference is small. Overall, we conclude from these tests that our model is not significantly affected by trade-offs with other depth ranges. This indicates that even though the *ScS* wave, which we used in inversions, may have sensitivity in regions shallower than our target depth range (Hung et al., 2005), the paths included in our data set do not sample significant anomalies in the shallow mantle. If anomalies would be present along these raypaths, not only the *ScS* but also the *S* wave would be affected even though the sensitivity of the *S* wave is different from that of the *ScS* wave. This is clearly not the case (Konishi et al., 2017).

5. Thermal and Compositional Changes From V_S and Q Anomalies

The deviations of V_S and Q from their PREM values that we observed may be related to local changes in temperature and possibly composition. To model the temperature changes associated with these anomalies, we follow the approach developed in Deschamps et al. (2019). For convenience, we summarize the main points below.

Taking into account the presence of postperovskite (pPv) and of compositional changes at the bottom of the mantle, the temperature anomalies associated with $d \ln V_S$, observed at a given location, may be written as

$$dT_{V_S} = \frac{d \ln V_S - S_{pPv} dX_{pPv} - d \ln V_{S,C}}{S_T} \tag{20}$$

where dX_{pPv} is the assumed anomaly (with respect to mantle horizontal average) in the fraction of pPv at this location, S_T and S_{pPv} are the partial derivatives (sensitivities) of V_S with respect to temperature and pPv, respectively, and $d \ln V_{S,C}$ is the contribution of compositional changes to $d \ln V_S$. If anomalies in V_S have a purely thermal origin, $d \ln V_{S,C}$ is, of course, equal to zero. By contrast, assuming as in section 5.2 that this contribution is dominated by changes in the iron fraction dX_{Fe}, this contribution can be written $d \ln V_{S,C} = S_{Fe} dX_{Fe}$, where S_{Fe} is the partial derivative (sensitivity) of V_S to iron. Other sources of chemical heterogeneities include variations in the fraction of subducted mid-ocean ridge basalts (MORB) and in the relative fractions of bridgmanite and ferropericlase. Here, we did not account these sources. If such chemical heterogeneities are present, our estimate of temperature may be altered (see discussion in Deschamps et al., 2019). Seismic sensitivities are calculated from available mineral physics data and appropriate equation of state modeling. Here, we use the sensitivities to temperature and iron calculated by Deschamps et al. (2012) together with their uncertainties. Note that because they derive from the kernels in traveltime and in amplitude (equations (10) and (11)), the values of $d \ln V_S$ we obtained are already corrected for the attenuation effects. Further correction, as done, for instance, in Matas and Bukowinski (2007) when using $d \ln V_S$ obtained from traveltime only, is therefore not needed. Based on the compilation of Cobden et al. (2015), we fixed the sensitivity of pPv to $S_{pPv} = (2.0 \pm 1.0)$. Equation (20) further requires the definition of a pPv model. pPv anomalies, dX_{pPv}, are set to -15% everywhere in the depth range 2,730–2,880 km. This assumes that the region we explored is hot and thus free of pPv and that the horizontally averaged fraction of pPv, $X_{pPv,ref}$, is equal to 15%, a value that is consistent with a CMB temperature around $T_{CMB} = 3500$ K (Deschamps et al., 2019). At shallower depths, pPv is assumed unstable everywhere in the mantle, that is, $dX_{pPv} = 0$. One may point out that this pPv model is rather simple and possibly bias our inferred values of dT_{V_S}. Using a more sophisticated radial model, where dX_{pPv} decreases with altitude according to prescribed Clapeyron slope, would slightly decrease the estimated values of dT_{V_S}, but the conclusion explaining $d \ln V_S$ requires that compositional changes would still be valid.

To estimate temperature anomalies associated with Q maps, we followed a classical approach, which assumes that attenuation is a thermally activated process with a relaxation time modeled with an Arrhenius law Anderson and Given (1982). In this approach, Q at a temperature T is described by a power law of the seismic frequency ω and the relaxation time and is given by

$$Q_S = Q_0 \omega^\alpha \exp\left(\alpha \frac{H}{RT}\right), \tag{21}$$

where Q_0 is a constant; α is the power law exponent; R the ideal gas constant; $H = E + pV$ the activation enthalpy, with E and V being, respectively, the activation energy and volume; and p is the pressure. Note that the activation volume is positive, that is, H increases with depth. Equation (21) may be used to define a reference quality factor, Q_{ref}, at a reference temperature T_{ref}, which we define here as PREM quality factor, $Q_{ref} = Q_{PREM} = 312$, and the mantle geotherm, respectively. The temperature deviation from T_{ref} at a given location, $dT_Q = (T - T_{ref})$, can be inferred from the ratio between Q_S and Q_{ref} following:

$$dT_Q = \frac{-RT_{ref}^2}{\alpha H} \frac{\ln\left(\frac{Q_S}{Q_{ref}}\right)}{\left[1 + \frac{RT_{ref}}{\alpha H}\ln\left(\frac{Q_S}{Q_{ref}}\right)\right]}. \tag{22}$$

This approach implicitly assumes that Q depends only on T, but not, or very weakly, on composition. Seismic attenuation may be affected by the presence of fluids—in particular water. Because the amount of water in the lowermost mantle is limited (Panero et al., 2015), this effect may however be very small. In addition, it has recently been suggested that the influence of volatiles on attenuation may be very small even at upper mantle conditions (Cline et al., 2018). Parameters of equation (22) for the lower mantle are uncertain. A conservative range for the reference temperature at the CMB is 3000–4000 K (Tackley, 2012). Following Deschamps et al. (2019), we fixed T_{ref} to 3500 K at the CMB and assumed that it decreases adiabatically with altitude following a gradient of 0.3 K/km. We further imposed a decrease by 500 K from the CMB up to the altitude of 200 km ($z = 2,680$ km) to account for the existence of a thermal boundary layer at the bottom of the mantle. Finally, we imposed an error bar of ± 500 K at each depth. For periods smaller than 200 s, seismic studies indicate that the frequency exponent α is around 0.3. Here, following Dannberg et al. (2017), we used $\alpha = 0.274$.

The two recent observational studies attempting to constrain alpha from seismic data find different results: At periods shorter than 200 s, Leki et al. (2009) find alpha of 0.3, while Hwang and Ritsema (2011) find alpha values closer to 0.1.

Finally, based on the experimental data compiled in Matas and Bukowinski (2007) and on the modeling of Dannberg et al. (2017), we set activation energy and volume to $E = 286$ kJ/mol and $V = 1.2 \times 10^{-6}$ m^3/mol, respectively, corresponding to a mean activation enthalpy of 450 kJ/mol at the bottom of the mantle. To estimate error bars on dT_Q, we varied E and V in the ranges 280–380 kJ/mol and 1.1×10^{-6}-1.3×10^{-6} m^3/mol, leading, at the bottom of the mantle, to activation enthalpy between 425 and 560 kJ/mol.

A successful thermochemical structure requires that, at a given location, estimates of the temperature anomalies from $d \ln V_S$ and Q are similar within error bars. Here, we quantify the difference between the two estimates with the misfit function

$$\chi = \frac{|dT_{V_S} - dT_Q|}{\sigma_{dT_{V_S}} + \sigma_{dT_Q}}, \tag{23}$$

where $\sigma_{dT_{V_S}}$ and σ_{dT_Q} are uncertainties in dT_{V_S} and dT_Q. With this definition, dT_{V_S} and dT_Q agree within their error bars if $\chi \leq 1$. By contrast, a value of χ larger than 1 indicates that dT_{V_S} and dT_Q are inconsistent. To infer the possible thermochemical structure in the region sampled by our model, we first assume that V_S changes are only thermal in origin (section 5.1). Because the resulting dT_{V_S} and dT_Q disagree ($\chi > 1$), we then assume that compositional changes are also present (section 5.2).

5.1. Purely Thermal Origin of $d \ln V_s$

Temperature anomalies estimated from our preferred models of $d \ln V_S$ and Q (Figure 4) are plotted in Figure 10. Values of dT_{V_S} assume a purely thermal origin of $d \ln V_S$, that is, $d \ln V_{S,C} = 0$ in equation (20). Patterns in dT_{V_S} and dT_Q mimic patterns in $d \ln V_S$ and Q. These are overall consistent with one another, with

strongest anomalies being located in the center of the explored region and amplitude of anomalies increasing from top to bottom. Details of the patterns are however slightly different. In particular, dT_{V_S} has sharper gradients than dT_Q. More importantly, dT_{V_S} and dT_Q strongly disagree in amplitude. In the lowermost layer, for instance, the root-mean-square (rms) amplitudes of dT_{V_S} and dT_Q are 700 and 240 K, respectively, and the maximum anomalies are around 860 K and 270 K.

Figure 11 plots maps of the misfit function χ (equation (23)). Uncertainties in dT_{V_S} are around 100 K and were estimated by adding estimated uncertainties in the observed $d \ln V_S$ (0.2%, section 4.1) and in seismic sensitivities. Uncertainties in dT_Q are typically around 150–200 K and were estimated by adding estimated uncertainties on the observed Q (± 15, section 4.1), T_{ref} (± 500 K), and H (see previous section). With these error bars, χ is larger than 1 throughout the region we explored in the bottom 300 km. At altitudes of 300–400 km above the CMB, estimated dT_{V_S} and dT_Q are closer to each other, with rms amplitude around 280 and 110 K. Within error bars, they are consistent in peripheral regions but still disagree in the central region. At altitudes larger than 500 km (not shown here), estimated dT_{V_S} and dT_Q are now in close agreement, with rms amplitude in the range 110–140 K and $\chi < 1$ in most of the explored region.

One may point out that χ is larger in the range 200–300 km above the CMB than in the lowermost layer. This is because in the lowermost 200 km, we assumed that parts of the anomalies in V_S are related to anomalies in pPv, while at shallower depths, we assumed that pPv is unstable whatever the location and therefore does not participate to V_S anomalies. Accounting for pPv anomalies in the lowermost layers thus reduces the difference between dT_{V_S} and dT_Q in these regions. In addition, because we imposed some uncertainty on the sensitivity of V_S to pPv, the uncertainty on dT_{V_S} increases. As a result, and according to equation (23), the value of χ in regions where pPv anomalies are accounted for is reduced.

Changing the damping factor modifies the amplitude of models of $d \ln V_S$ and Q. While these changes are small (Figure 7), they may affect estimated temperature anomalies. Figure S8, plotting temperature anomalies estimated from the model weakly damped model shown in Figure 7, then indicates that dT_Q is larger than those predicted by our preferred model by up to 150 K. However, as indicated by Figure S9, dT_Q is still in disagreement with dT_{V_S} throughout the bottom 300 km

Following this approach, and assuming that Q does not depend on composition, the disagreement between estimated dT_{V_S} and dT_Q in the lowermost 300 km indicates that the $d \ln V_S$ we observe in this region is not purely thermal in origin and is partially caused by compositional changes. Note that because activation energies for bridgmanite and ferropericlase are different—typically around $E_{\text{Bm}} = 300$ kJ/mol and $E_{\text{Fp}} = 230$ kJ/mol at ambient pressure (Yamazaki & Irifune, 2003; Yamazaki et al., 2000)—variations in the relative fraction of these minerals should lead to small changes in Q. In particular, if LLSVPs are enriched in bridgmanite by a few percent (Trampert et al., 2004), the activation enthalpy should be larger than the mean value assumed in our calculations. However, according to equation (22), this would further decrease the estimated value of dT_Q, which would then be even more difficult to reconcile with the estimated dT_{V_S}. This would further implicitly assume that the $d \ln V_S$ we observe results partly from compositional changes. Another source of uncertainty is the reference fraction of pPv, which we fixed here to 15%. If higher, around 50% and more, dT_Q and dT_{V_S} may be reconciled for a narrow range of values of the reference temperature (see discussion).

5.2. Compositional Changes

Assuming that they are only related to thermal changes and associated depletion in pPv, the temperature anomalies we estimated from $d \ln V_S$ in the lowermost 300 km are too large compared to those we estimated from Q. A possible explanation for this disagreement is that the region sampled by our data set has a different composition than the surrounding mantle and that these compositional anomalies participate to the observed $d \ln V_S$. An excess of iron is a reasonable explanation for such anomalies, as it would induce a decrease in V_S and an increase in density, as seen in normal mode tomography (Ishii & Tromp, 1999; Moulik & Ekstrøm, 2016; Trampert et al., 2004). Other possible sources of heterogeneities that may contribute to the observed $d \ln V_S$ are subducted oceanic crust (MORB) and an enrichment in bridgmanite. Subducted MORB may reach the bottom of the mantle and be partially incorporated within LLSVP (Li et al., 2014; Tackley, 2012). However, because V_S increases with increasing fraction of MORB (Deschamps et al., 2012), the presence of recycled MORB in the western Pacific would imply that the dT_{V_S} calculated from our observed $d \ln V_S$ is even larger than the values we obtained and thus more difficult to reconcile with the estimated dT_Q. Excess in bridgmanite would lead to similar effects.
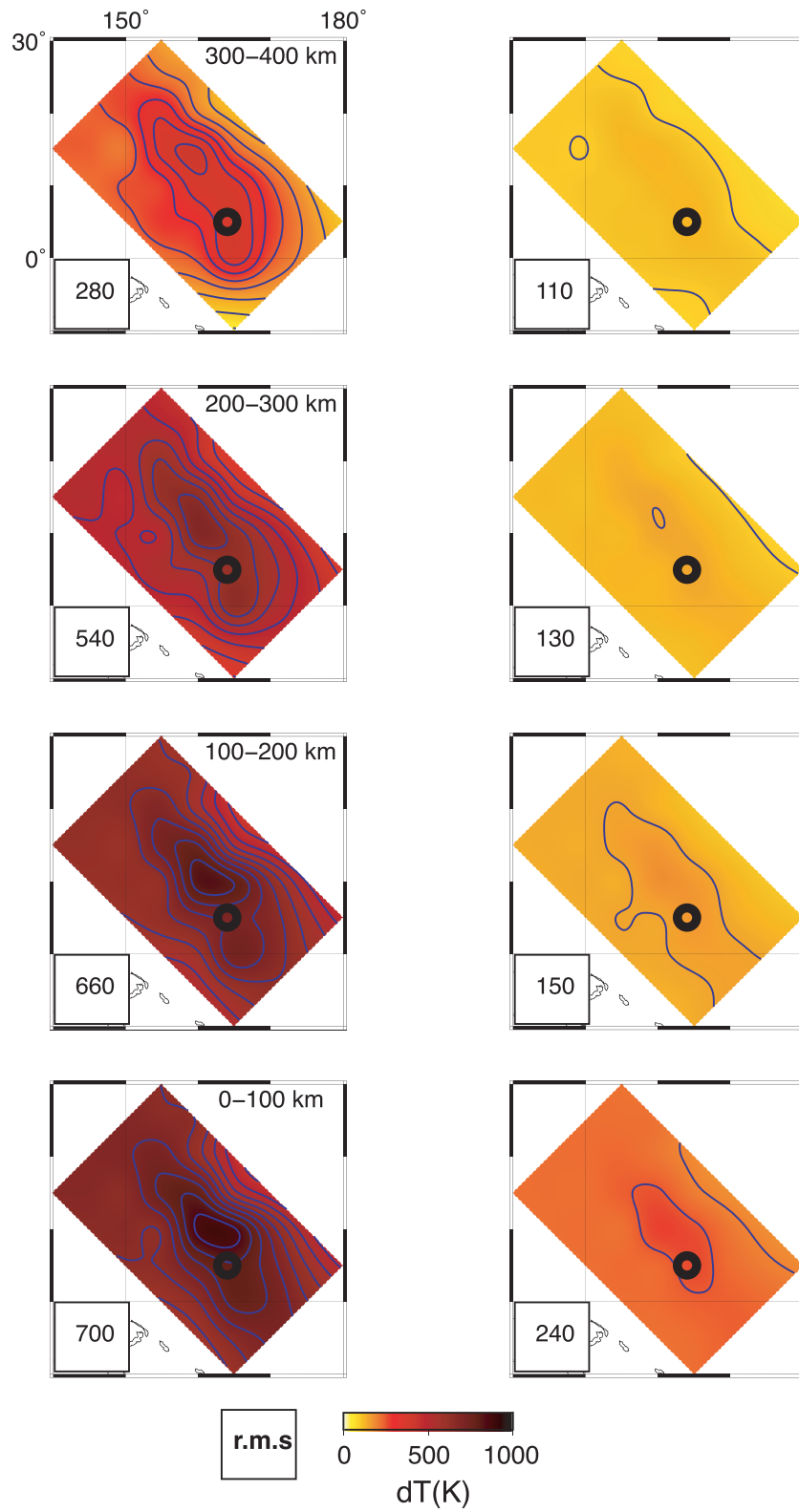
Figure 10. Temperature anomalies estimated via (left) $d \ln V_S$ and (right) Q. The contour interval is 50 K. The insets at the top right of the dT_{V_S} maps indicate the elevation range above the CMB. The insets at the bottom left show the rms values in dT_{V_S} and dT_Q.
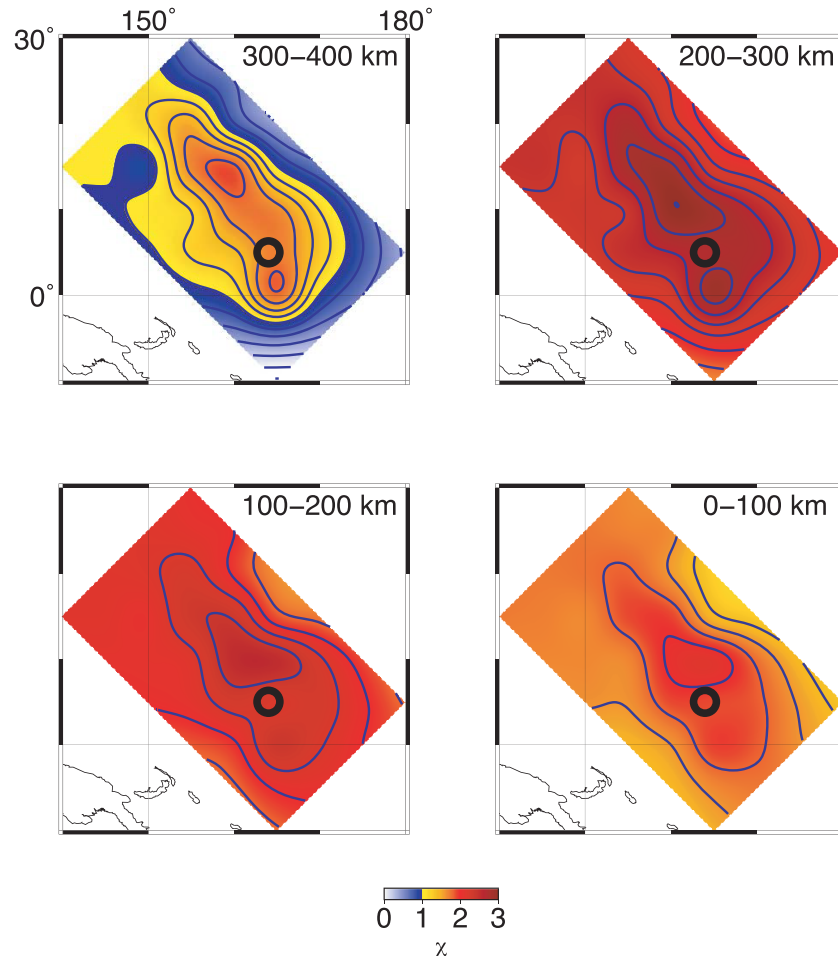
Figure 11. Distribution of the cost function χ (equation (23)). The contour interval is 0.2. The inset at the top right indicates the elevation range above the CMB.

Here, we assume that compositional changes in the region we explored, if present, are dominated by an excess in iron oxide, dX_{Fe}. Following this hypothesis, and assuming that the temperature anomalies are well described by dT_Q, the iron excess is given by

$$dX_{Fe} = \frac{d\ln V_S - dT_Q S_T - dX_{pPv} S_{pPv}}{S_{Fe}},\qquad(24)$$

where the functions S_T, S_{Fe}, and S_{pPv} are, again, partial derivatives (sensitivities) of V_S with respect to temperature, iron, and pPv, respectively. Figure 12 shows the resulting maps of dX_{Fe}. Inferred iron excess in the lowermost 300 km is on average 3.5–4.5%, depending on depth, with error bars around 1.2–2.8%. Note that the strongest iron enrichments are located in the central part of the explored region.

We further calculated temperature anomalies from the $d\ln V_S$ and Q models obtained from the bootstrap tests plotted in Figure S2. Figure S8 shows differences between these anomalies and those predicted by the preferred model (Figure 4). We found that differences in temperature anomalies are very small, less than 20 K for dT_{V_S} and less than 3 K for dT_Q. Differences in the estimated iron excess (see section 5.2) are also small, less than 0.25%.

6. Discussion and Conclusion

To better constrain the nature of the Pacific LLSVP, we inferred the 3-D structure of shear velocity anomalies ($d\ln V_S$) and seismic quality factor (Q) at the western tip of this region using a finite-frequency tomography method. The resulting models of $d\ln V_S$ and Q have similar patterns; that is, the variations in $d\ln V_S$ and Q
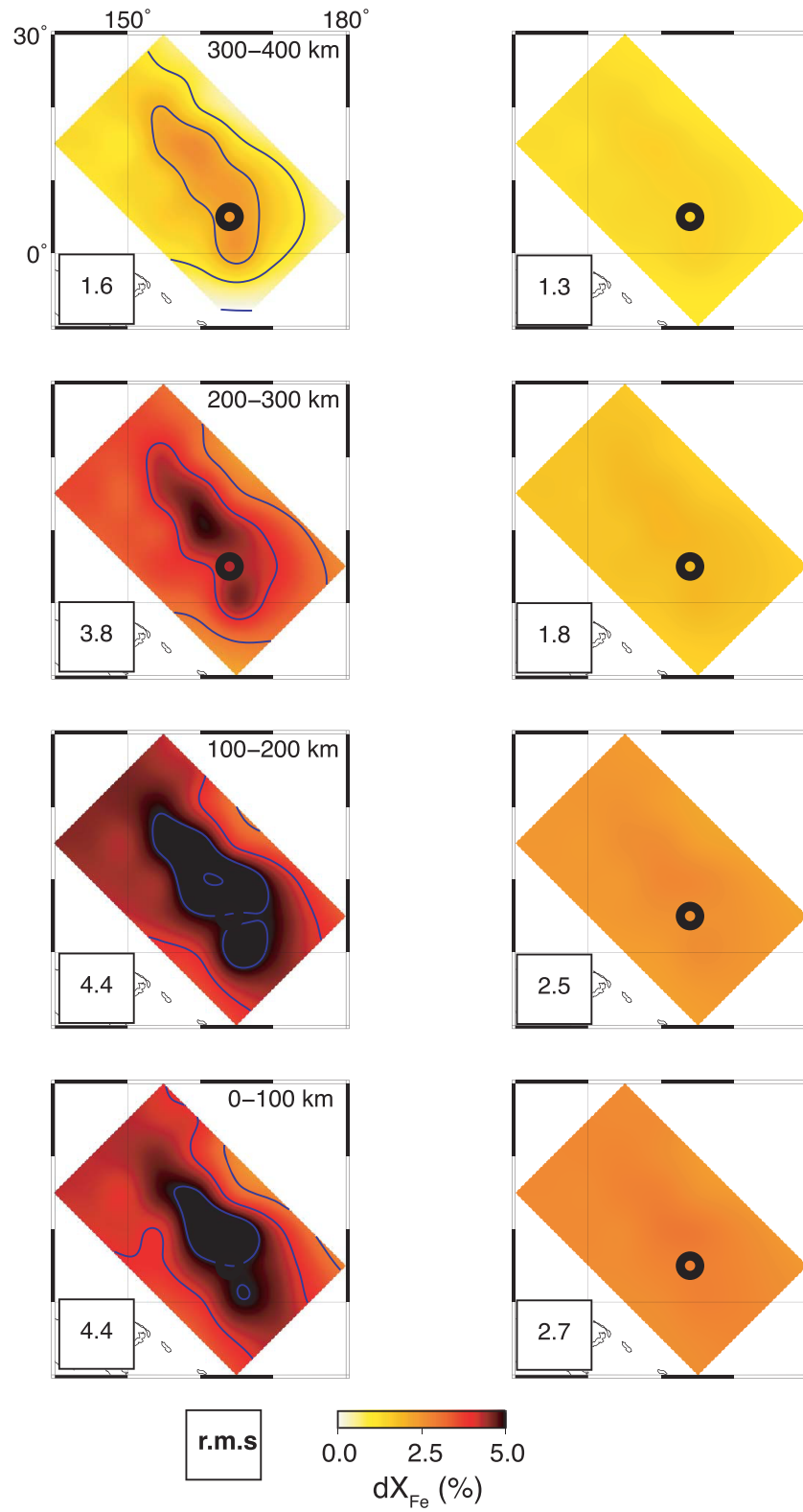
Figure 12. Average (left column) and standard deviation (right column) estimated from residual $d \ln V_S$ (equation (24)). The contour interval is 1%. Inset at the top right of each map indicates the elevation range above the CMB. Inset at the bottom left shows the rms values of their respective map.

are strongly correlated. Throughout the region we explored, V_S and Q are substantially lower than those in PREM. At all depths, lowest values are found around 10°N, 160°E, which approximately correspond to the surface location of the Caroline plume. This feature fully agrees with the 1-D models obtained in Konishi et al. (2017). Another observation is that the amplitudes of anomalies in V_S and Q are strongest in the bottom 200 km and regularly decrease upward.

The target region was set to the lowermost 500 km in the mantle, and we assumed that the upper part does not affect the seismic data much because S waves data have no significant difference from PREM (Konishi et al., 2017). Additional tests performed in this study (section 4.5) validate this assumption. We imposed this limitation in the explored depth range first because the initial model we used, taken from Konishi et al. (2017), is defined in the lowermost 900 km of the mantle and second because 3-D resolution may not be good enough in regions above.

The strong deviations in V_S and Q compared to PREM suggest that the region we explored is affected by important thermochemical changes with respect to average mantle. A key result is that the temperature anomalies predicted independently by our models of $d \ln V_S$ and Q are not consistent. In the lowermost 100 km, temperature anomalies predicted by changes in $d \ln V_S$ are larger than those estimated from Q by 460 K on average, a difference that cannot be reconciled within error bars. Estimates from $d \ln V_S$ and Q can be reconciled only in the shallowest part of our model. Interestingly, our estimates of temperature anomalies from Q are lower than those obtained in the African LLSVP by Liu and Grand (2018), a difference due to the fact that this study observes very low values of Q in this region, around 110. In contrast to our findings, Liu and Grand (2018) estimates of temperature in the African LLSVP are in agreement with estimates from $d \ln V_S$ in this region and therefore support a purely thermal nature of this structure. If both our estimates of Q and that of Liu and Grand (2018) are correct, this may indicate that the two LLSVPs are different in nature or in their evolution stage. More likely, differences in the observed Q may be related to differences in the method employed to measure attenuation and/or to the fact that the seismic phases used in Liu and Grand (2018) and in our study are different. Assuming that Q is only sensitive to temperature and that the discrepancy between the estimated dT_{V_S} and dT_Q results from an enrichment in iron in the explored region, we calculated the amount of iron needed to explain the observed $d \ln V_S$ and Q (Figure 12). In the lowermost 300 km, explaining the $d \ln V_S$ we observe requires 4–5% iron excess compared to surrounding mantle.

Our modeling of Q includes several sources of uncertainties that we discussed in section 5.1. It further assumes that Q depends only on temperature, and not, or very weakly, on composition. If Q depends on composition, the temperature anomalies deduced from observed Q may change, and at least part of the discrepancies between estimated dT_{V_S} and dT_Q may be related to the fact that our observed Q is affected by compositional effects that we do not account for. This case, however, implicitly assumes that compositional changes are needed to explain observed $d \ln V_S$ and Q simultaneously; that is, the conclusion that $d \ln V_S$ cannot be explained by purely thermal changes remains valid *de facto*. A possible source of chemical dependence of attenuation is that activation energies of bridgmanite and ferropericlase are different. If, as suggested by probabilistic tomography (Mosca et al., 2012; Trampert et al., 2004), LLSVPs are enriched in bridgmanite, activation energy of LLSVP material would be different from that of surrounding mantle. Assuming that activation energies of bridgmanite and ferropericlase are equal to $E_{Bm} = 300$ and $E_{Fp} = 230$ kJ/mol (Yamazaki & Irifune, 2003; Yamazaki et al., 2000), respectively, and defining the activation energy of the aggregate as the of harmonic average of E_{Bm} and E_{Fp}, activation energies for regular mantle (assumed to be pyrolitic, with 80% bridgmanite) and LLSVP enriched material (with 90% bridgmanite) are around 283 and 291 kJ/mol, respectively. At lowermost mantle conditions, this leads to activation enthalpies of 440 kJ/mol for regular material and 450 kJ/mol for material enriched in bridgmanite. Following equation (22) and taking $T_{ref} = 3500$ K and $\alpha = 0.274$, temperature anomalies for regular and enriched materials differ by only 10 K for $Q = 200$ and 5 K for $Q = 250$. It is further important to note that dT_Q is smaller for $H = 450$ kJ/mol than for 440 kJ/mol, that is, dT_Q would be slightly more difficult to reconcile with dT_{V_S} if an enrichment in bridgmanite is accounted for. Thus, lateral variations in the fraction of bridgmanite, even if affecting attenuation, would not substantially affect our estimates of temperature anomalies. Another potential source of chemical heterogeneities in the lowermost mantle is the presence of recycled oceanic crust, as slabs may sink down to the CMB (e.g., van der Hilst et al., 1997). In addition small fractions of recycled crust may be incorporated in LLSVP (Li et al., 2014; Tackley, 2012). In the absence of measurements for the activation energy for MORB, it is however difficult to estimate the effect of recycled oceanic crust on our observed Q. The presence of recycled MORB in the region sampled by our model may further affect V_S. However, this would slightly increase V_S

in this region (Deschamps et al., 2012), that is, have the opposite effects of an excess in temperature and/or iron. Accounting for the presence of MORB would thus increase the temperature excess compared to our estimates of dT_{V_S}, further increasing the discrepancy between dT_{V_S} and dT_Q. Another source of uncertainty is the value of the reference (horizontally averaged) fraction of pPv in the lowermost mantle.

This parameter may be estimated from the CMB temperature and from the maximum amplitude of temperature variations in the lowermost mantle (Deschamps et al., 2019). The value we assumed in our calculations, $X_{pPv,ref} = 15\%$, is based on the assumption that the CMB temperature, T_{CMB}, is equal to 3500 K and that the maximum amplitude of temperature anomalies is $\pm$ 500 K. If this temperature is lower, pPv may be stable over wider regions, and $X_{pPv,ref}$ may be larger. The anomaly in the fraction of pPv in the region we sample, dX_{pPv}, may then increase, in which case its contribution to the observe $d\ln V_S$ would be larger, resulting in larger estimated dT_{V_S}. However, according to equation (21) decreasing T_{CMB} would also cause dT_Q to decrease. In addition, if T_{CMB} is low enough, pPv may be stable even in the region we explore, reducing dX_{pPv} at this location. A detailed calculation accounting for these effects (Deschamps et al., 2019) then shows that for T_{CMB} in the range 2800–3200 K, and for the parameter values we used, estimated dT_Q and dT_{V_S} may be reconciled within their error bars. It should be pointed out that these values of T_{CMB} are on the lower end of its estimated possible range.

The bootstrap test we conducted (section 4.3) indicates that our data set is robust and that the inverted values of $d\ln V_S$ and Q are only affected by small errors. Due to the subjectivity in defining the optimal regularization, our preferred models of $d\ln V_S$ and Q (Figure 4) are only possible ones among others. Interestingly, the structures we observe are also stable with respect to regularization. When less damping is applied (Figure 7), Q is overall smaller than in our preferred model, but the difference remains small, with rms and minimum Q around 240 and 220 in our preferred model and 230 and 200 in the model with less damping.

This further affects estimates of dT_Q, which are larger than that of our preferred model by about 150 K (Figure S8), but it does not change the conclusion that compositional anomalies are needed to explain observed $d\ln V_S$ and Q (Figure S9).

While the 3-D pattern for our model of $d\ln V_S$ and Q remains overall robust across a variety of inversion setup, its precise outline and absolute values should be investigated more in detail, in particular to obtain better estimates of error bars from uncertainties in the data and changes of model parameters. Monte Carlo methods are well suited to explore seismological structure with such a wide range of parameter spaces and yields of stochastic objectivity in results. They produce full probability density functions, rather than single values, at each point of the model, which can then be used to estimate trade-offs and uncertainties in the output model. Finally, output models obtained via Monte Carlo methods are less affected by the initial model than those obtained by inverse problems. Models of $d\ln V_S$ and Q based on Monte Carlo inversion should thus provide finer mapping of deep mantle seismic structures and more accurate information of their nature.

References

Anderson, D. L., & Given, J. W. (1982). Absorption band Q model for the Earth. *Journal of Geophysical Research*, *87*(B5), 3893–3904. https://doi.org/10.1029/JB087iB05p03893

Azimi, S. A., Kalinin, A. V., Kalinin, V. V., & Pivovarov, B. B. (1968). Impulse and transient characteristics of media with linear and quadratic absorption laws. *Izvestiya - Physics of the Solid Earth*, *2*, 88–93.

Cline, C. J., Faul, H. U., David, E. C., Berry, A. J., & Jackson, I. (2018). Redox-influenced seismic properties of upper-mantle olivine. *Nature*, *555*, 355–358.

Cobden, L. J., Thomas, C., & Trampert, J. (2015). Seismic detection of post-perovskite inside the Earth. In A. Khan, & F. Deschamps (Eds.), T*he Earth's heterogeneous mantle* (pp. 391440). Springer. https://doi.org/10.1007/978-3-319-15627-9&urluscore;13

Dannberg, J., Eilon, Z., Faul, U., Gassmöller, R., Moulik, P., & Myhill, R. (2017). The importance of grain size to mantle dynamics and seismological observations. *Geochemistry, Geophysics, Geosystems*, *18*, 3034–3061. https://doi.org/10.1002/2017GC006944

Davies, R. D., Goes, S., Davies, J. H., Schuberth, B. S. A., Bunge, H.-P., & Ritsema, J. (2012). Reconciling dynamic and seismic models of Earth's lower mantle: The dominant role of thermal heterogeneity. *Earth and Planetary Science Letters*, *353–354*, 253–269. https://doi.org/10.1016/j.epsl.2012.08.016

Deschamps, F., Cobden, L., & Tackley, P. J. (2012). The primitive nature of large low shear-wave velocity provinces. *Earth and Planetary Science Letters*, *349-350*, 198–208. https://doi.org/10.1016/j.epsl.2012.07.012

Deschamps, F., Konishi, K., Fuji, N., & Cobden, L. (2019). Radial thermo-chemical structure beneath western and northern Pacific from seismic waveform inversion. *Earth and Planetary Science Letters*, *520*, 153–163. https://doi.org/10.1016/j.epsl.2019.05.040

Deschamps, F., Li, Y., & Tackley, P. (2015). Large-scale thermo-chemical structure of the deep mantle: Observations and models. In A. Khan, & F. Deschamps (Eds.), *The Earth's Heterogeneous Mantle*, (pp. 479–515). Springer. https://doi.org/10.1007/978-3-319-15627-9&urluscore;15

Fuji, N., Kawai, K., & Geller, R. J. (2010). A methodology for inversion of broadband seismic waveforms for elastic and anelastic structure and its application to the mantle transition zone beneath the Northwestern Pacific. *Physics of the Earth and Planetary Interiors*, *180*(3–4), 118–137. https://doi.org/10.1016/j.pepi.2009.10.004

Garnero, J. E., McNamara, K. A., & Shim, S.-H. (2016). Continent-sized anomalous zones with low seismic velocity at the base of Earth's mantle. *Nature Geoscience*, *9*, 481–489. https://doi.org/10.1038/ngeo2733

Geller, R. J., & Hara, T. (1993). Two efficient algorithms for iterative linearized inversion of seismic waveform data. *Geophysical Journal International*, *115*(3), 699–710. https://doi.org/10.1111/j.1365-246X.1993.tb01488.x

Geller, R. J., & Ohminato, T. (1994). Computation of synthetic seismograms and their partial derivatives for heterogeneous media with arbitrary natural boundary conditions using the Direct Solution Method. *Geophysical Journal International*, *116*(2), 421–446. https://doi.org/10.1111/j.1365-246X.1994.tb01807.x

Geller, R. J., & Takeuchi, N. (1995). A new method for computing highly accurate DSM synthetic seismograms. *Geophysical Journal International*, *123*(2), 449–470. https://doi.org/10.1111/j.1365-246X.1995.tb06865.x

He, Y., & Wen, L. (2009). Structural features and shear-velocity structure of the Pacific anomaly. *Journal of Geophysical Research: Solid Earth*, *114*, B02309. https://doi.org/10.1029/2008JB005814

Houser, C., Masters, G., Shearer, P., & Laske, G. (2008). Shear and compressional velocity models of the mantle from cluster analysis of long-period waveforms. *Geophysical Journal International*, *174*(1), 195–212. https://doi.org/10.1111/j.1365-246X.2008.03763.x

Hung, S.-H., Garnero, E. J., Chiao, L.-Y., Kuo, B.-Y., & Lay, T. (2005). Finite frequency tomography of d shear velocity heterogeneity beneath the caribbean. *Journal of Geophysical Research*, *110*, B07305. https://doi.org/10.1029/2004JB003373

Hwang, Y. K., & Ritsema, J. (2011). Radial q structure of the lower mantle from teleseismic body-wave spectra. *Earth and Planetary Science Letters*, *303*(3), 369–375. https://doi.org/10.1016/j.epsl.2011.01.023

Ishii, M., & Tromp, J. (1999). Normal-mode and free-air gravity constraints on lateral variations in velocity and density of earth's mantle. *Science*, *285*, 1231–1236. https://doi.org/10.1126/science.285.5431.1231

Konishi, K., Deschamps, F., & Fuji, N. (2017). Elastic and anelastic structure of the lowermost mantle beneath the Western Pacific from waveform inversion. *Geophysical Journal International*, *208*(3), 1290–1304. https://doi.org/10.1093/gji/ggw450

Konishi, K., Fuji, N., & Deschamps, F. (2019). *3-D elastic and anelastic structure of the lowermost mantle beneath the Western Pacific*[Data set]. *Zenodo*. https://doi.org/10.5281/zenodo.3491418

Konishi, K., Kawai, K., Geller, R. J., & Fuji, N. (2014). Waveform inversion for localized three-dimensional seismic velocity structure in the lowermost mantle beneath the western pacific. *Geophysical Journal International*, *199*(2), 1245–1267. https://doi.org/10.1093/gji/ggu288

Kustowski, B., Ekström, G., & Dziewoński, A. M. (2008). Anisotropic shear-wave velocity structure of the Earth's mantle: A global model. *Journal of Geophysical Research*, *113*, B06306. https://doi.org/10.1029/2007JB005169

Leki, V., Matas, J., Panning, M., & Romanowicz, B. (2009). Measurement and implications of frequency dependence of attenuation. *Earth and Planetary Science Letters*, *282*(1), 285–293. https://doi.org/10.1016/j.epsl.2009.03.030

Li, M., McNamara, A. K., & Garnero, E. (2014). Chemical complexity of hotspots caused by cycling oceanic crust through mantle reservoirs. *Nature Geoscience*, *7*(5), 366–370. https://doi.org/10.1038/ngeo2120

Liu, C., & Grand, S. P. (2018). Seismic attenuation in the african LLSVP estimated from PCS phases. *Earth and Planetary Science Letters*, *489*, 8–16. https://doi.org/10.1016/j.epsl.2018.02.023

Matas, J., & Bukowinski, S. T. M. (2007). On the anelastic contribution to the temperature dependence of lower mantle seismic velocities. *Earth and Planetary Science Letters*, *259*, 51–65.

Minster, B., & Anderson, D. (1981). A model of dislocation-controlled rheology for the mantle. *Philosophical Transactions of The Royal Society A: Mathematical, Physical and Engineering Sciences*, *299*, 319–356. https://doi.org/10.1098/rsta.1981.0025

Mosca, I., Cobden, L., Deuss, A., Ritsema, J., & Trampert, J. (2012). Seismic and mineralogical structures of the lower mantle from probabilistic tomography. *Journal of Geophysical Research*, *117*, B06304. https://doi.org/10.1029/2011JB008851

Moulik, P., & Ekström, G. (2016). The relationships between large-scale variations in shear velocity, density, and compressional velocity in the Earth's mantle. *Journal of Geophysical Research: Solid Earth*, *121*, 2737–2771. https://doi.org/10.1002/2015JB012679

Panero, W. R., Pigott, J. S., Reaman, D. M., Kabbes, J. E., & Liu, Z. (2015). Dry (Mg,Fe)SiO3 perovskite in the Earth's lower mantle. *Journal of Geophysical Research: Solid Earth*, *120*, 894–908. https://doi.org/10.1002/2014JB011397

Panning, M., & Romanowicz, B. (2006). A three-dimensional radially anisotropic model of shear velocity in the whole mantle. *Geophysical Journal International*, *167*(1), 361–379. https://doi.org/10.1111/j.1365-246X.2006.03100.x

Ritsema, J., Deuss, A., van Heijst, H. J., & Woodhouse, J. H. (2011). S40RTS: A degree-40 shear-velocity model for the mantle from new Rayleigh wave dispersion, teleseismic traveltime and normal-mode splitting function measurements. *Geophysical Journal International*, *184*(3), 1223–1236. https://doi.org/10.1111/j.1365-246X.2010.04884.x

Simmons, N. A., Forte, A. M., & Grand, S. P. (2009). Joint seismic, geodynamic and mineral physical constraints on three-dimensional mantle heterogeneity: Implications for the relative importance of thermal versus compositional heterogeneity. *Geophysical Journal International*, *177*(3), 1284–1304. https://doi.org/10.1111/j.1365-246X.2009.04133.x

Tackley, P. J. (2012). Dynamics and evolution of the deep mantle resulting from thermal, chemical, phase and melting effects. *Earth-Science Reviews*, *110*(1), 1–25. https://doi.org/10.1016/j.earscirev.2011.10.001

Takeuchi, N. (2012). Detection of ridge-like structures in the Pacific large low-shear-velocity province. *Earth and Planetary Science Letters*, *319–320*, 55–4. https://doi.org/10.1016/j.epsl.2011.12.024

Takeuchi, N., Morita, Y., Xuyen, N. D., & Zung, N. Q. (2008). Extent of the low-velocity region in the lowermost mantle beneath the western Pacific detected by the Vietnamese broadband seismograph array. *Geophysical Research Letters*, *35*, L05307. https://doi.org/10.1029/2008GL033197

To, A., Romanowicz, B., Capdeville, Y., & Takeuchi, N. (2005). 3D effects of sharp boundaries at the borders of the African and Pacific superplumes: Observation and modeling. *Earth and Planetary Science Letters*, *233*(1), 137–153. https://doi.org/10.1016/j.epsl.2005.01.037

Trampert, J., Deschamps, F., Resovsky, J., & Yuen, D. (2004). Probabilistic tomography maps chemical heterogeneities throughout the lower mantle. *Science*, *306*(5697), 853–856. https://doi.org/10.1126/science.1101996

van der Hilst, R., Widiyantoro, S., & Engdahl, E. (1997). Evidence for deep mantle circulation from global tomography. *Nature*, *386*, 578–584.

Yamazaki, D., & Irifune, T. (2003). Fe-Mg interdiffusion in magnesiowüstite up to 35 GPa. *Earth and Planetary Science Letters*, *216*(3), 301–311. https://doi.org/10.1016/S0012-821X(03)00534-X

Yamazaki, D., Kato, T., Yurimoto, H., Ohtani, E., & Toriumi, M. (2000). Silicon self-diffusion in MgSiO3 perovskite at 25 GPa. *Physics of the Earth and Planetary Interiors*, *119*, 299–309. https://doi.org/10.1016/S0031-9201(00)00135-7